Eur. J. Mech. B - Fluids 20 (2001) 771–797

S0997-7546(01)01141-4/FLA

Experimental and numerical investigation of nonlinear thermocapillary oscillations in an annular geometry

Renaud Lavalley, Gustav Amberg *, Henrik Alfredsson

Department of Mechanics, KTH, 100 44 Stockholm, Sweden

(Received 17 December 1998; revised 24 October 2000 and 14 March 2001; accepted 11 April 2001)

Abstract – The present work investigates thermocapillary flow in a cylindrical configuration using large Prandtl number liquids. The flow is studied using coordinated simulations and experimental optical methods such as PIV and flow visualization. In this way, properties of the oscillatory state can be obtained in great detail. Considerable attention is given to the search for the parameters influencing the onset of the instability. It is found that the onset of oscillations can be correlated using a thermocapillary Reynolds number. The oscillations take the form of a standing wave close to the onset, which is replaced by a travelling wave for stronger forcing. The selection of azimuthal wave number of the oscillatory mode is determined from geometrical parameters, and resembles the wave number selection in vortex ring instabilities. Throughout we obtain good agreement between experiments and simulations using a mathematical model with an undeformed adiabatic free surface. © 2001 Éditions scientifiques et médicales Elsevier SAS

thermocapillar / surface-tension / convection / stability / DNS / PIV

1. Introduction

In materials science, many manufacturing processes involve melting and solidification. The flow that occurs in the melt during these processes plays a crucial role for the properties of the finished product. There are a number of possible driving forces which may cause motion in the melt, such as gravitational buoyancy, Lorentz forces and thermocapillary forces, i.e. thermally induced variations of surface tension on a fluid interface. The latter will be particularly important in applications such as crystal growth and welding, where a free surface subject to intense temperature gradients is present. Under micro-gravity conditions in space, or with small dimensions on earth, the thermocapillary forces turn out to be the dominating cause of fluid motion (see the low-gravity fluid flow review by Ostrach [1], and the recent review of thermocapillary experiments by Schatz and Neitzel, [2]). In semiconductor crystal growth processes, notably the float-zone method, the dopant is often found concentrated in a regular banded structure called striations, which is caused by an oscillatory convection driven by surface-tension gradients during the growth of the crystal. This technical problem has inspired numerous recent studies on onset of oscillations in basic thermocapillary convection.

Much of the theory of stability of thermocapillary flows starts from the work by Davis and coworkers, [3–7]. Smith and Davis, [3,4], investigated the linear stability of two-dimensional liquid layers with infinite horizontal extent, subject to a horizontal temparature gradient. They identified an instability that has been termed the ‘hydrothermal wave’, which takes the form of a temperature-disturbance wave that propagates in a direction which depends on the Prandtl number. The instability mechanism was explained by Smith [7] for the small and large *Pr* limits in terms of the interaction between the thermal field and the inertially (low *Pr*)

* Correspondence and reprints.
E-mail address: gustava@mech.kth.se (G. Amberg).

or viscously (high Pr) dominated flow. Smith and Davis [4] also found another kind of instability, the 'surface wave instability', which could become critical for zero horizontal flow rate and a Prandtl number less than 0.15. Xu and Davis [5,6] examined the axisymmetric version of this problem, i.e. the stability of the thermocapillary flow in an infinitely long liquid bridge. Recently the first experimental demonstration of the hydrothermal wave instability in plane geometries was made by Riley and Neitzel [8].

The study of the float-zone configuration has been simplified by the use of the half-zone model. The half zone consists of two cylindrical rods with flat end faces maintained at different temperatures and located at a distance from each other. The gap between the two cylinders is filled with a liquid drop which is held in place by surface tension forces. The onset of oscillations in half-zones have been studied experimentally [9,10], by full numerical simulations in 3D [11,12], and by linear stability [13], to mention only a few. The mechanism for the onset of oscillatory flow at low Prandtl number has been identified by Levenstam and Amberg [12] as a purely hydrodynamic instability, very similar to the instability of a vortex ring. At Prandtl numbers greater than unity, Wanschura et al. [13] identified the instability as a modified thermocapillary wave.

Another geometry where the dynamics have similarities with the half zone is the annular geometry studied in this paper. In this case, a cylindrical container with a small co-axial cylindrical heater is used. The fluid is contained in the annular gap between the heater and the container wall. A free surface subjected to a radial gradient of temperature is hence created. Kamotani et al. [14] were the first to experimentally study a thermocapillary flow in a cylindrical container of the annular type. This geometry is attractive since it presents many experimental advantages, and the dynamics can be expected to be similar to other axisymmetric thermocapillary convection cases. Kamotani et al. used a 2 cSt silicone oil with a Prandtl number equal to 27. Over a threshold difference of temperature they obtained a 3D oscillatory thermocapillary flow with a periodic surface temperature pattern. A first set of microgravity experiments were carried out in 1992, [15–17], where the steady thermocapillary flow was investigated. A numerical study of the steady axisymmetric flow is compared to PTV (Particle Tracking Velocimetry) and temperature measurements. More recent microgravity experiments by Kamotani et al. [18–20] investigated the onset of oscillations in this geometry. A 2 cS silicone oil with Prandtl number around 27 was used in cylindrical containers with diameters 1.2, 2 and 3 cm. The temperature distribution on the free surface was measured for oscillatory flows. The deformation of the free surface during oscillations was also measured. The influence of buoyancy on the surface-tension driven convection in cylindrical containers was studied experimentally by Kamotani et al. [21–23] and numerically by Bäuerle [24].

The group of Kamotani and Ostrach have in the series of papers referenced above observed critical temperature differences for onset of oscillations that they claim are not consistent with a critical Marangoni number. This is problematic, since, if thermocapillarity is the important physical mechanism, the only independent nondimensional parameters are the Marangoni number and the Prandtl number. Thus, for experiments using the same fluid, the onset would be expected to be specified by a certain critical value of the Marangoni number, $Ma = \gamma \Delta T R/(\mu\alpha)$. This would imply for instance that the critical temperature difference ΔT would be inversely proportional to the size of the container (R). However, the experiments of Kamotani, Ostrach and coworkers have shown a weaker dependence of ΔT on R. In the first ground based experiments [14], they found a critical ΔT that was independent of size, while in the evaluation of the recent space experiments [18] they suggested that the critical ΔT was proportional to $R^{-1/2}$.

To explain this they have argued that free surface deformations are important and have proposed a mechanism for the instability that relies on the coupling between the thermocapillary heat transfer and a time dependent surface deformation. This would indeed introduce a new physical mechanism, and an additional nondimensional number, that would allow a weaker dependence of critical temperature difference on size. They have also argued that a similar mechanism would be important in the half-zone geometry [25].

However, this explanation is not without problems, and has not been generally accepted. The first observation is that the time dependent surface deformations that are observed during oscillations are very small. Kamotani et al. [18] measured the surface deflections in their microgravity experiment and state that "The amplitude of free surface deformation was a few microns near the onset of oscillations and increased to several microns at higher ΔT". This amplitude was apparently comparable to random surface deformations caused by residual gravity. Furthermore the maximum amplitude is said to occur away from the heater, outside the half-radius point. These observations contradict the proposed instability mechanism, where the free surface motions are supposed to interact with the thermocapillary flow 'near the heater'. It is also hard to believe that these really minute surface deformations should be anything else than a secondary response to the oscillations that does not have much dynamic significance, especially since the onset seems well defined despite superimposed random surface motions of a similar magnitude. In the half zone case there have been several reasonable comparisons between experiments and stability calculations that assume an undeformed free surface, [13,26,27]. We are not aware of any published direct comparisons between stability theory and experiments for the cylindrical container geometry. We can only conclude that the instability mechanism is still obscure, and that more work is needed.

Here we present a detailed study of the properties of critical and supercritical oscillatory flow in the cylindrical container geometry. By complementary simulations and experiments we can both verify our simulations and experiments, and obtain a complete picture of the supercritical oscillatory state. In section 2 the simulation model is described, in section 3 the experimental procedures are discussed. Different aspects of the flow are discussed using joint observations from experiments and simulations in section 4.

2. Mathematical model and numerical method

Thermocapillary flows are driven by the variation of surface tension with temperature, which will be assumed to follow a linear relation,

$$\sigma = \sigma_0 - \gamma(T - T_0), \tag{1}$$

where T_0 is a reference temperature and γ a constant for a given liquid. Surface tension usually decreases with increasing temperature, so γ is expected to be positive.

The geometry studied here is presented in *figure 1*. It is a cylindrical cell of radius R and height H open at the top with a co-axial heater of radius R_h. The geometrical parameters are thus the aspect ratio $h = H/R$ and the ratio of the inner and outer cylinder radii $a = R_h/R$. The heater and the outer wall are at different constant temperatures, T_h and T_w. A radial temperature gradient is thus imposed and the surface tension gradient will cause fluid near the surface to flow from the warm co-axial pipe towards the cold wall, setting up a toroidal vortex in the cell.

The numerical model takes buoyancy and thermocapillary effects into account. The fluid is treated as a Boussinesq one with constant dynamic viscosity μ, constant thermal diffusivity α and a constant density ρ_0 except for the buoyancy term where the density is allowed to vary.

The problem is made nondimensional by scaling lengths with the container radius R, time with R/U, and velocities with the thermocapillary velocity scale $U = (\gamma \Delta T)/\mu$, where μ is the dynamic viscosity and γ is defined in equation (1). The nondimensional temperature is defined as $\theta = (T' - T_w)/(T_h - T_w)$, and density and pressure are scaled with ρ_0 and $\rho_0 U^2$ respectively, with ρ_0 denoting the density at the reference temperature, T_w in this case.

The nondimensional equations thus become

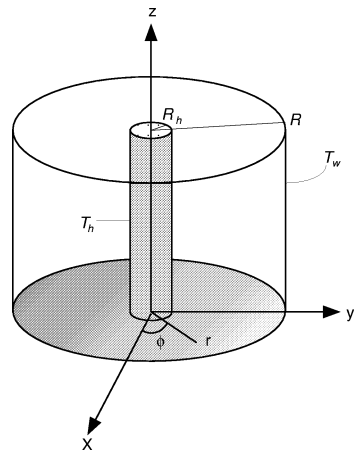

Figure 1. Geometry.

$$\nabla \cdot \mathbf{u} = 0, \tag{2}$$

$$\frac{\partial \mathbf{u}}{\partial t} + (\mathbf{u} \cdot \nabla)\mathbf{u} = -\nabla p + \frac{1}{Re}\nabla^2 \mathbf{u} - \frac{Gr}{Re^2}\theta \cdot \mathbf{e}_z, \tag{3}$$

$$\frac{\partial \theta}{\partial t} + \mathbf{u} \cdot \nabla\theta = \frac{1}{Re\,Pr}\nabla^2\theta. \tag{4}$$

The Reynolds, Prandtl and Grashof numbers, *Re*, *Pr* and *Gr*, are defined according to:

$$Re = \frac{U \cdot R}{\nu} = \frac{\gamma \Delta T R}{\nu \mu}, \tag{5}$$

$$Pr = \frac{\nu}{\alpha}, \tag{6}$$

$$Gr = \frac{\beta g \Delta T R^3}{\nu^2}, \tag{7}$$

where α is the thermal diffusivity, β is the coefficient of thermal expansion, ν the kinematic viscosity, and g the gravitational acceleration.

As an alternative to the Reynolds number, a Marangoni number is often used:

$$Ma = Re \cdot Pr = \frac{\gamma \Delta T R}{\mu \alpha}. \tag{8}$$

The thermal conditions are assumed to be an adiabatic bottom, and prescribed temperatures at the heater and the cylindrical container wall. At the free surface there is a possibility for heat loss to the ambient air, and a thermal boundary condition representing this was implemented. However, numerical simulations for the estimated largest possible heat loss clearly showed that this was negligible in our experiments. We will thus in the following only report on simulations assuming an adiabatic free surface.

Moreover, the free surface is modeled as flat and undeformed, ruling out surface deformations in the numerically observed oscillations.

The velocity boundary conditions are no-slip on the wall, heater and bottom. On the free surface the surface tension variation with temperature will give rise to the usual thermocapillary coupling between shear stress and temperature gradient.

The mathematical expression of these boundary conditions are:

$$\mathbf{u} = \mathbf{0}, \qquad \theta = 0 \quad \text{at } r = 1, \tag{9}$$

$$\mathbf{u} = \mathbf{0}, \qquad \theta = 1 \quad \text{at } r = a, \tag{10}$$

$$\mathbf{u} = \mathbf{0}, \qquad \frac{\partial \theta}{\partial z} = 0 \quad \text{at } z = 0, \tag{11}$$

$$\frac{\partial u}{\partial z} = -\frac{\partial \theta}{\partial x}, \qquad \frac{\partial v}{\partial z} = -\frac{\partial \theta}{\partial y}, \qquad w = 0, \qquad \frac{\partial \theta}{\partial z} = 0 \quad \text{at } z = h. \tag{12}$$

2.1. Numerical method

A numerical solver developed by Levenstam [28] and based on a finite element formulation was used to solve the system of equations. The elements used are three dimensional brick elements with 27 nodes. The formulation is iso-parametric so that the geometry is transformed using the same base functions as for the unknowns, giving an accurate treatment of the curved boundaries. The code uses piecewise quadratic polynomials as base functions. This is a higher order accurate method and third order accuracy is obtained. A Galerkin approach has been used to formulate the discrete equations for the unknowns.

The time discretisation is implicit in the viscous term and explicit in the convective ones. With this implementation one linear system of equations for each velocity component and the temperature together with the Poisson equation for the pressure has to be solved in every time step. The linear systems that arise are solved by a conjugate gradient method with an incomplete Cholesky decomposition as a preconditioner. The explicit treatment of the convection terms impose a restriction of the timestep, a CFL condition needs to be satisfied by the timestep to achieve stability. This yields smaller timesteps with increasing Reynolds number. The time necessary to simulate the equivalent of one second in an experiment, but a typical simulation time for a well overcritical case was about 13 hours whereas the simulation of a low Reynolds number could be as small as 2.5 hours on a SUN Ultra workstation.

2.2. Code validation

The computer code has been thoroughly tested by Levenstam [28] and comparisons with numerical computations in a two dimentional cavity by Zebib et al. [29] showed excellent agreement as well as the half-zone model computations by Shen et al. [30].

Bäuerle [24] built the grid for the configuration studied here and investigated carefully how the elements should be distributed in order to give accurate results for high Prandtl numbers. The choice of a highly stretched mesh was governed by the need of high grid resolution near the heater and the cold wall. The influence of grid resolution on velocities in the container is 4% between the grid listed in *table I*, for the even more demanding case of $Pr = 27$.

The grid chosen for our simulations was primarily the third one in *table I*, $20 \times 12 \times 16$, which had the smallest Δr. The vertical resoluton is 0.0042 near the free surface, which, in view of the third order accurate numerics, is sufficient to resolve the thermal boundary layer.

The influence of the grid resolution in the azimuthal direction was also checked for a representative simulation. Two simulations of the same case with different number of nodes were performed. *Figure 2* shows

Table I. Results on different grids, $Pr = 27$, $Re = 1400$, $Gr = 1300$, from [24]. $\Delta r_{\min}$ and $\Delta z_{\min}$ denote the minimal grid spacings in the radial and axial directions, respectively. $u_{\max}$ and $w_{\max}$ are the maximal velocity magnitudes in the radial and axial diretions.

Grid($n_r \times n_\phi \times n_z$)	$\Delta r_{\min}$	$\Delta z_{\min}$	$u_{\max}$	$w_{\max}$
$16 \times 10 \times 14$	0.0082	0.0058	0.0805	0.0283
$20 \times 12 \times 16$	0.0062	0.0049	0.0806	0.0284
$20 \times 12 \times 16$	0.0025	0.0042	0.0777	0.0295
$24 \times 12 \times 20$	0.0050	0.0038	0.0799	0.0291

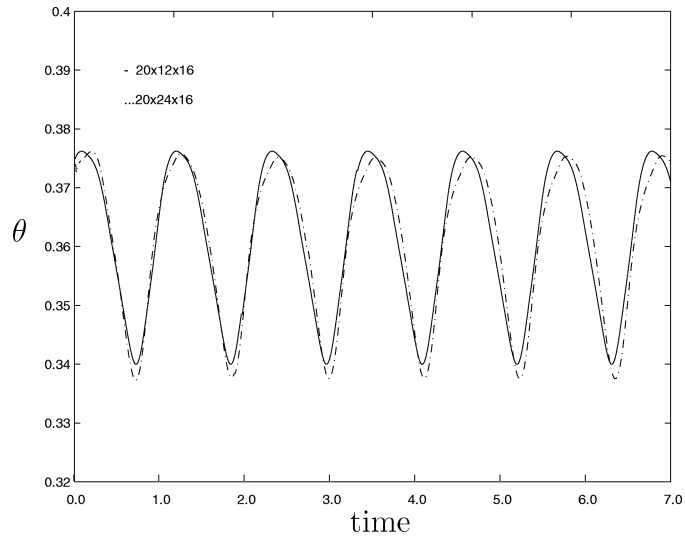

Figure 2. Surface temperature at $r = 0.49$, for $Pr = 14$, $Re = 4650$, $a = 0.21$, $h = 1$. Solid line: $20 \times 12 \times 16$, dashed line: $20 \times 24 \times 16$.

the temperature at one point at $r = 0.49$ and $z = 1$ for a representative oscillatory case, as a function of time. Results for this case are shown in *figures 16* and *17* below. Doubling the azimuthal resolution generates a variation in the amplitude of the oscillations of 4.5% of the amplitude. Note that the amplitude of the oscillation is in itself very small (~ 0.035) compared to the temperature variation in the base flow (~ 1). The accuracy in terms of variation with mesh refinement is thus 4.5% of 0.035, i.e. 0.16%. We can conclude that the mesh with 12 nodes in the azimuthal direction is quite sufficient to resolve the oscillations that are present in these flows.

The crucial property of the present method that allows this accuracy even with so few nodes, is that it represents the unknowns as piecewise quadratic functions. There is a tremendous increase in numerical accuracy, when replacing more conventional second-order schemes (standard finite volume and finite difference formulations for instance) by a higher order of accuracy method. In our experience this is necessary for accurate high Prandtl number simulations.

3. Experimental equipment and procedure

The test fluid is contained in a cylindrical container with a central heating cylinder. The container side wall is maintained at a low temperature by circulating water from a low temperature bath, whereas a warm temperature bath provides hot water which flows through the central pipe. Two different cells were used, test cell I is made of copper whereas cell II is partially transparent. The two test cells are part of different experimental setups,

where cell I is employed in setups for temperature measurements and visualization from the top, and cell II is used to visualize a vertical section and for PIV measurements.

3.1. Experimental test cell I

A drawing of test cell I is shown in *figure 3*. It consists of a 3 mm inner radius (R) copper cylinder, a pipe made of stainless steel of radius $R_h = 0.5$ mm, co-axial with the cylinder, and an insulating insert made of Teflon which provides a near adiabatic boundary condition at the bottom of the cell.

The water cooling of the copper wall yields an approximately uniform, constant-temperature boundary condition. Similarly, water from a constant temperature bath circulates through the co-axial pipe ensuring a constant-temperature heater on the axis of the test cell. The temperature drop over the pipe wall is easily estimated, and, making the conservative assumption that the temperature variation outside the heater occurs over a length comparable to the pipe wall thickness (~ 0.1 mm), the temperature drop will be of the order $k_{\text{oil}}/k_{\text{wall}} \cdot (T_h - T_w)$. Even though stainless steel is a poor heat conductor compared to other metals, it has a much higher heat conduction coefficient than the high-Prandtl number silione oil, and the temperature drop over the wall is less than 1% of the total temperature drop.

The Teflon insert at the bottom can slide vertically, allowing the aspect ratio A to be variable. To minimize the disturbances at the free surface due to transient laboratory air currents, a cylindrical Plexiglas 'windscreen' is installed around the flow cell at the top of the apparatus. The 'windscreen' was preferred to a lid because of condensation problems at the cold surface on the lid.

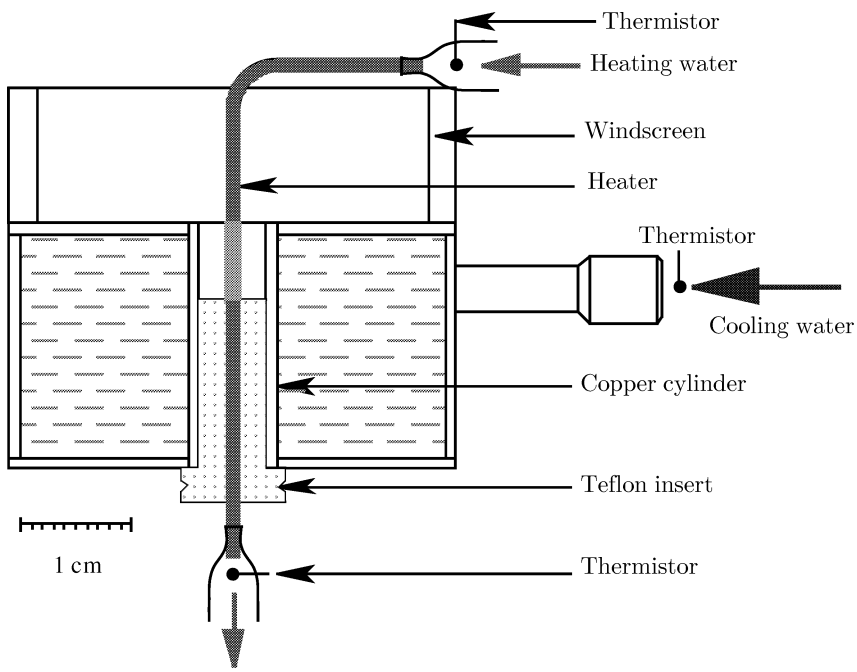

Figure 3. Test cell I.

3.2. Experimental test cell II

The geometry of the second test cell is similar to that of test cell I, however the outer cooling system was designed with the objective to allow flow visualization and PIV measurements on a vertical section of the cell. Cut views of the test cell is shown in *figure 4*. The cell consists of a 2.67 mm radius glass cylinder with a Teflon insert which can slide inside the glass cylinder allowing a variable aspect ratio. A small hole of 0.5 mm diameter was made through the Teflon insert to allow filling up the cell with silicone oil without disturbing the surface with a needle as with the copper apparatus. This was a necessary step since the flat surface condition was more difficult to obtain than for the test cell I.

The cylinder is placed in a square cavity made of PVC in which the cooling water circulates (see *figure 5*). One side of the cavity is transparent to allow visualization. Due to the planar walls of the PVC cavity, the image distortion at the passage from water to air is eliminated. There is however an unavoidable distortion when light rays pass from the cylindrical test cell, through the wall of the glass cylinder, and into the water bath. The refractive indices of silicone oil and water are quite close, $n_{\text{water}} = 1.33$ and $n_{\text{silicone}} = 1.38$, and the glass wall is thin (0.4 mm thickness with refractive index $n_{\text{glass}} = 1.5$), so this is a minor problem. The optical path was computed taking into account the passage through water, glass and silicone oil. This shows that the maximal distortion occurs for a particle viewed at a distance $0.81R$ from the axis, where its true position is displaced outwards by 7.1% of the radius, compared to the position that would be inferred from a linear interpolation on a raw image.

3.3. Temperature measurement technique

Temperature measurements in the test cell were performed using a cold wire technique, where the principle is to have a constant current passing through a tiny platinum wire. The wire acts as a resistance thermometer and the voltage is then directly proportional to the temperature. In order to measure the temperature fluctuation without contamination by the velocity fluctuation the resistance-wire should be operated with as low current as possible. In the experiments the current was limited to 0.3 mA, which gave a heating power of at most a few μW. Moreover since silicone oil has excellent dielectric properties the wire could be introduced in the oil without any insulating protection.

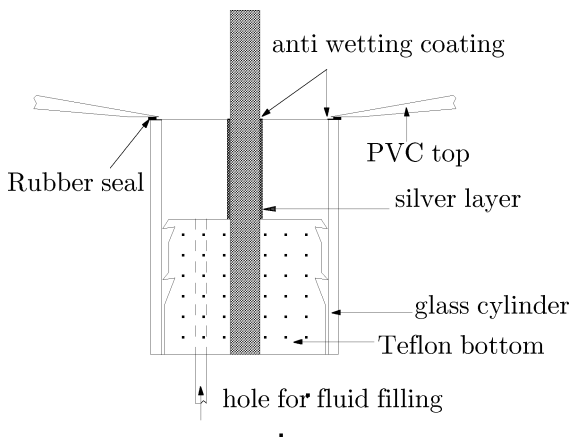

Figure 4. Enlargement of the test cell II.

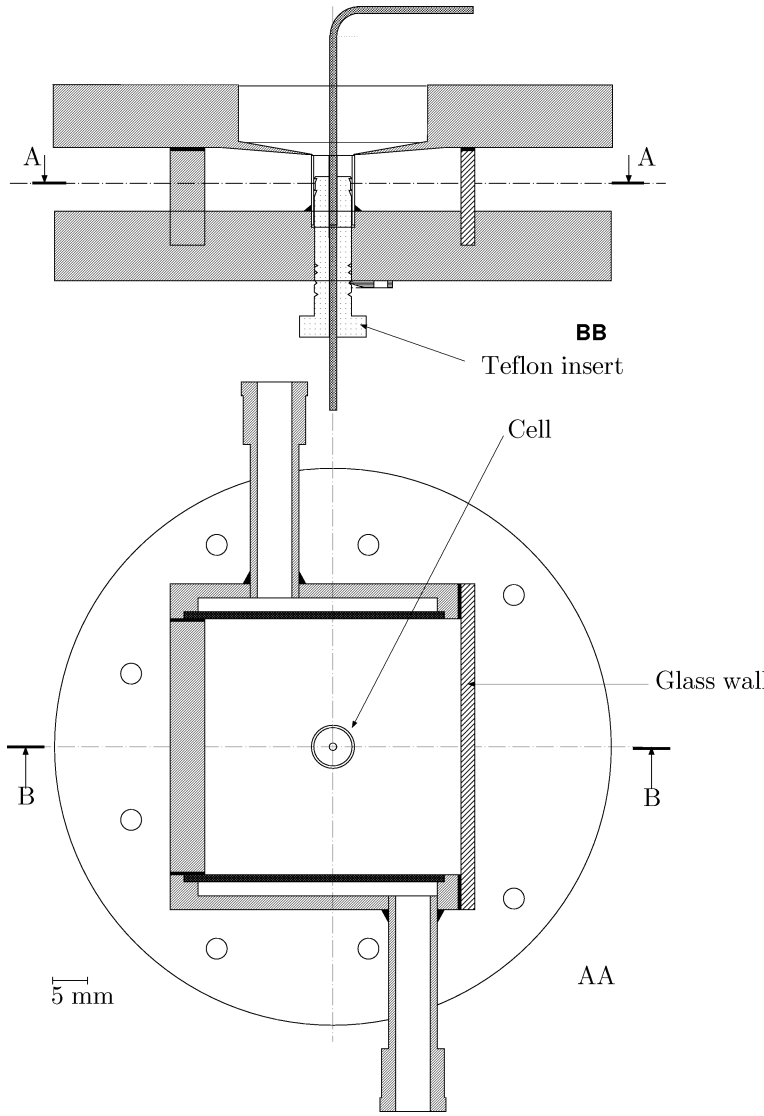

Figure 5. Cut views of the test cell II.

The probe has a special design to minimize the disturbance of the flow when introducing it through the surface of the liquid. It was manufactured by us from 2.5 μm diameter 10% Rodium–Platinum wire with a working length of 0.5 mm. The wire is introduced ortogonal to the flow direction because the temperature gradient is reasonably small in that direction. The temperature probe can be positioned accurately with a micromanipulator (Research Instrument Limited). The possible perturbations generated by introduction of the wire at the surface were expected to be damped within a few seconds. The probe is connected to an AN-1003 anemometer (AALab Systems Ltd). The signal from the anemometer is filtered (1st-order filter with a cutoff frequency of about 15 Hz) and sampled with a cutoff frequency of 48 Hz using a Mac Adios A/D converter and recorded on a Macintosh II. The cold wire technique allows very small dimensions for the measuring probe and a very short time response, well within what is required here, see [31] for details.

3.4. Flow visualization

With test cell I flow visualization of horizontal sections was made. A microscope (Olympus SZ-6045TR) was used to view the cell from above. The flow was seeded with a large amount of flakes (Irodin 120 Pearl Lustre). In addition a focusing below the surface permits the capture of the oscillation of the toroidal vortex. With fewer flakes and a focus on the back flow, it is possible to determine the onset of oscillation by following the particle paths which becomes wavy. A CCD video camera was connected to the microscope and sequences of different cases were recorded on a Hi8 video recorder.

Flow visualization using test cell II was aimed at making streamline visualizations of the flow in a vertical section of the cell. This method was only used for a steady state flows, when streamlines can be visualized by particle paths. The fluid was seeded with spherical metallic coated particles from TSI usually employed for LDV (Laser Doppler Velocimetry). Their density is 2.8 g/cm^3 with an average diameter of 4 μm with a very small size variation. Two microscopes were used to access both the liquid surface and the cell side. A 35 mm camera was connected to the side microscope and a picture was taken with a long shutter time. The light sheet was created using a Xenon arc lamp together with a fiber optic arm and a slit, which was 0.5 mm wide and was placed 2 mm from the liquid surface.

3.5. Particle image velocimetry

The instrumentation used for the present study is a system developed by Dantec (Flowmap PIV2000 for the processor). The light sheet illumination is provided by a Nd:YAG laser (Spectra Physics), with a wavelength of 532 nm (green light). The circular light beam is converted to a light sheet with a thickness of 0.3 mm. The illumination system is so powerful that the question of the laser influence upon the liquid surface temperature field arises. An estimate (see [31] for details) yields that the heating by the laser of the liquid surface is of the order of few hundredths of a degree. The influence is hence negligible. A CCD camera (Kodak Megaplus ES 1.0) with 1008×1018 resolution is used. The camera captures two consecutive images that are coordinated with laser bursts, before transferring the information to the processor. The minimum time between 2 frames is 1 μs. The time delay chosen in our case is between 1 and 2 ms.

The step following the frame grabbing is the correlation processing. The two frames are divided in a number of interrogation areas, which in our measurement is 64×64 pixels with 50% overlap. The physical size of the interrogation area varies beteween various measurements and are given when the results are presented. The software FlowManager from Dantec is used to analyse the raw data and extract velocity fields.

The seeding of the flow is of great importance for the quality of PIV measurements. Each particle should be at least 3 pixels in diameter on the recorded images, and they should be uniform in size. The amount of seeding is governed by the need to have 5 to 10 particles per interrogation region, and it is important that the particle distribution in the fluid is uniform if the whole field is to be resolved. In our PIV measurements the silicone oil has been seeded with the same particles as used for side visualization.

In section 3.2, the optical distortion due to the imperfect match of the refractive indices of water and silicone oil was discussed. Since this was a small source of error we did not attempt to correct for this in the PIV evaluation. The distortion was an outward displacement of at most 3% of the radius, which would give an error of similar magnitude in the velocity data in the bulk flow, where velocity gradients are order unity.

Table II. Physical properties of silicone oil at 25°C.

ν (cSt)	ρ (kg/m^3)	β (K^{-1})	σ (N/m)	γ (N/mK)	k (W/mK)	C_p (J/kgK)	Pr
1.00	818	0.00134	$17.2 \cdot 10^{-3}$	$7.55 \cdot 10^{-5}$	0.10	1716	14.0

3.6. Fluid properties

The working liquid used is Dow Corning 200 1 cSt silicone oil. The physical properties were mostly obtained from the manufacturer, with the exception of the surface tension and the viscosity. The basic properties are listed in *table II*. Information about the temperature dependence of the surface tension was obtained from [8], independent measurements by Johansson [32] gave similar values.

The viscosity data supplied by the manufacturer was checked using a U-tube microviscometer which, at 25°C, gave 1.03 cSt for the nominal 1 cS oil. The temperature dependence of the viscosity was taken into account in the experiments. From the manufacturer specifications a simple function was fitted to the data

$$\nu = 1.003 \cdot 10^{-6} - 1.15 \cdot 10^{-8}(T - T_0)\ \mathrm{m}^2/\mathrm{s}. \tag{13}$$

This implies a decrease by 10% between 20 and 30°C. The remaining properties (except surface tension) are assumed constant.

3.7. Experimental conditions

The importance of buoyancy forces compared to thermocapillary forces can be estimated from the equations and a criterion for when buoyant forces are important can be written as

$$\frac{Gr}{Re^{4/3}} = \frac{Bo_d}{Re^{1/3}} < 1. \tag{14}$$

Here $Bo_d = Gr/Re = \rho g \beta R^2/\gamma$. This estimate is derived from the usual estimate of boundary layer thickness and velocity magnitude in the thermocapillary boundary layer, and a comparison of the buoyant term in the momentum equation, to the remaining terms, [17,21,22,33]. In the recent space experiments by Kamotani et al. [18], it seems clear that for container diameters around 1 cm or less, gravity does not influence the results, but for larger containers is does. Evaluating the left-hand side of criterion (14) for their data, we obtain a value of $Gr/Re^{4/3} = 0.24$ for their 1 cm diameter container, 0.07 corresponding to the 0.5 cm diameter, and 0.81 for the 2 cm diameter. We will thus infer that $Gr/Re^{4/3} \leqslant 0.24$ is a precise criterion for neglecting buoyancy.

In our case $Bo_d = 1.28$, and a typical Reynolds number is above 3000, which, for $h = 1$, implies that $Gr/Re^{4/3} = Bo_d/Re^{1/3} \leqslant 0.089$. Thus, according to the findings from the space experiments [18], buoyancy should be of minor importance in our experiments.

In order to prevent the silicone oil from wetting the upper surfaces of the container and the heater, the dry surfaces were coated with Fluorad (3M Scotchguard). This procedure allows the free surface to attach to the container and the heater along well controlled contact lines. To provide a sharp corner where the surface attaches to the heater, a silver layer was soldered on the heater surface and machined to match the cell height. The heater radius is increased that way by 0.135 mm. Taking the increase in radius due to the silver layer into account, a becomes 0.21. The rim of the layer is also coated with Fluorad. This design fixes the positions of

the contact lines and allows a free surface that is perfectly flat, as far as can be determined optically, over the entire area.

To obtain the heater temperature, two thermistors were placed at the entrance and the exit of the pipe passing through the cell. The heater temperature is assumed to be the average of the temperature of these two thermistors. The flow rate was large enough (>1 cm/s) to provide a temperature drop between the thermistors of less than 1°C. Moreover the temperature uniformity along the heater's immersed part was estimated to be better than 0.1°C. The wall temperature was measured using a thermistor at the exit of the cold water circulation chamber. The high velocity in the chamber allowed the temperature of the wall to be measured with an error less than 0.1°C. This procedure together with the thermistor uncertainty gave the temperature difference $\Delta T = T_h - T_w$ with an uncertainty of ± 0.2°C. This means a temperature variation of less than 2% between the entrance and the exit in terms of the total temperature difference across the test cell.

The outer cylinder of test cell I was made of copper and the temperature drop across the wall was very small. In test cell II the outer cylinder was made of glass, and the low thermal conductivity of glass made it necessary to use a cylinder as thin as possible to minimize the temperature drop between the inner and the outer sides. The glass cylinder that was used had a wall thickness of 0.42 mm, giving an estimated temperature drop over the glass wall of 0.5 ± 0.2°C for a difference of 20°C between the heater and the cooling fluid.

3.8. Experimental procedure

Before any measurements a number of preparations were necessary. First the test cell was cleaned with alcohol and then with acetone. The container and the heater rims were recoated with Fluorad to fulfill the non-wetting condition. The silicone oil was filtered, and the test cell was filled using a syringe until a flat surface was achieved. A waiting period of a quarter of an hour was observed for the fluid to reach a thermal equilibrium, before the fluid level was carefully adjusted.

For temperature measurements the probe was brought to the desired position using the micromanipulator and microscope and after a period of about 1 minute (to allow possible perturbations due to the wire to be damped out) the sampling of the signal was started. The sampling time was chosen short (20 s) so that the evaporation was negligible but long enough to get an accurate value for the oscillation amplitude.

To avoid any influence from the transient increase of the temperature difference the heater temperature was increased in steps of 1°C with a slow heating ramp of about 0.1°C/min until instabilities occurred. The steps were then reduced to 0.2°C starting from a steady case.

After any change in temperature the system was allowed to equilibriate for 10 min. This time is long compared to the thermal diffusion time $R^2/\alpha \approx 100$ s.

4. Results

4.1. Steady basic flow

To show the characteristics of the steady basic flow, coordinated simulations, PIV-measurements and visualizations were made for a typical subcritical flow at a Reynolds number of $1.2 \cdot 10^3$, corresponding to a temperature difference of 5°C. The fluid mean temperature was in the experiment chosen to be 25°C, which gives an average viscosity of 1 cSt and Prandtl number of 14, as used in the simulation. Streak visualisation of the streamlines of the right side of the cell is presented in *figure 6*. Following the procedure described in section 3.4 the picture was taken with 1 second exposure which clearly shows the streamline pattern.

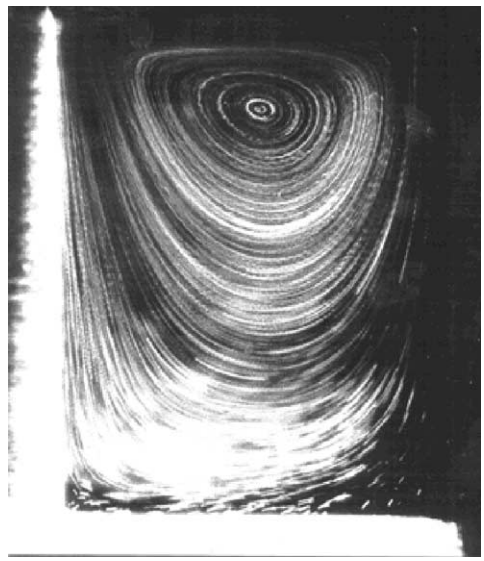

Figure 6. Streamline visualization of the right side of the vertical section of the cell, $a = 0.21$, $\Delta T = 5°\text{C}$, $Pr = 14$.

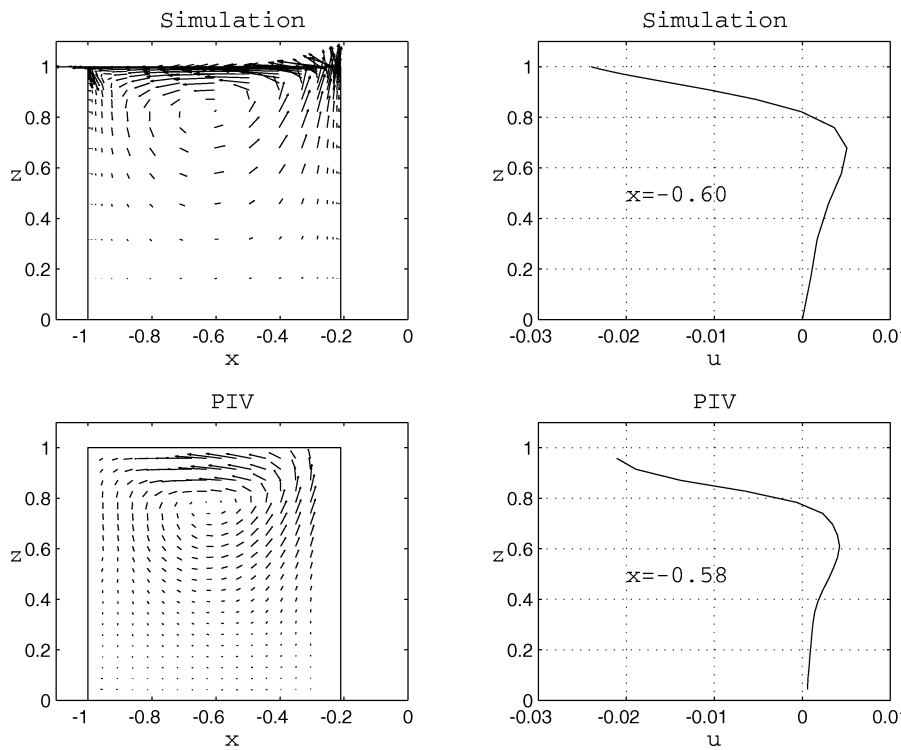

Figure 7. Nondimensional velocity in the left side section of the cell, simulation and PIV, $a = 0.21$, $Re = 1235$, $Pr = 14$. Interrogation area is 64×64, corresponding to 0.25 by 0.25 mm^2.

Velocity fields in a vertical section of the left side of the cell, obtained from simulations and PIV, are shown in *figure 7*. Even quantitatively the features of the vortex are in good agreement between the PIV and the numerical simulation, although there is a slight shift downwards for the velocity profile obtained in the PIV-measurements, which may be due to uncertainty in determining the precise location of the free surface in the experiment. There is also a difference in the shape of the velocity profiles near the free surface. This is due to difficulties in the PIV measurements very close to the free surface, where the interrogation area (0.25 mm $\times$ 0.25 mm) becomes comparable to the distance to the free surface. Also, the region very close to the surface was shadowed by a rubber seal between the PVC and the glass cylinder (see *figure 4*).

In the PIV measurements the extrapolation of the velocity to the surface gives a dimensional velocity estimate of 1.3 cm/s at $r = 0.6$. At the same radius the maximum velocity of the backflow is 2 mm/s. The difference of one order of magnitude between the surface velocity and the back velocity shows again that the flow is of thermocapillary origin.

In all, the good agreement between the measured and computed velocity fields in *figures 6* and *7*, strongly supports our confidence in the calibration of the experiments and the validations and accuracy of the simulations.

4.2. Onset of oscillations

Increasing the difference in temperature across the liquid surface above a threshold ΔT_{cr}, or equivalently a critical Reynolds number Re_{cr}, will cause the flow to bifurcate into an oscillatory state. The primary means for determining this critical Reynolds number was cold-wire temperature measurements, as described in section 3.3. According to bifurcation theory the amplitude of the surface temperature fluctuations is proportional to the square root of $\Delta T - \Delta T_{cr}$, for a supercritical bifurcation near the critical point. Hence the measurement of the temperature oscillations for slightly supercritical cases allows us to extrapolate to zero amplitude and obtain the critical difference of temperature for the onset of the oscillations. This method was used for comparisons between experiments and simulations. A visual method of determining the threshold was also used. The flow was then visualized with tracer particles and observed from above through a microscope. The temperature difference was varied in steps until the threshold had been localized with sufficient accuracy.

The shape of the free surface was found to be quite important for the value of the critical Reynolds number, in agreement with for instance Kamotani et al. [34], who found that the base flow velocities in the corners were changed drastically when the surface shape was altered. Here, a series of qualitative experiments were made in test cell I with aspect ratio $h = 2.2$. The surface shape was altered by changing the volume of liquid in the cell. It was found that the flow is destabilized by increasing the volume, i.e. making the surface convex, and stabilized by a concave shape. The critical Reynolds number would typically differ by say 25% between a flat and an either concave or convex surface.

The influence of the surface shape has recently been investigated for half zones by Sumner et al. [35], using both experiments and energy stability theory. It is interesting to note that the trend that we find experimentally in this geometry seems to match what Sumner et al. find theroetically for the half zone; a decreasing critical Marangoni or Reynolds number with inreasing volume, and conversely. However, in the liquid bridge, their extensive experiments show instead that the straight cylindrical shape (corresponding to a flat surface in this geometry) is the most stable shape, with significantly lower critical temperature differences for both convex and concave cross sections.

The influence of the aspect ratio on the critical Reynolds number for the onset of the oscillations is shown in *figure 8*. The critical Reynolds number decreases with increasing h for $h < 1$. The bottom of the cell induces a retardation of the flow and tends to stabilize it. For an aspect ratio of 1.5 and higher the trend is opposite. This

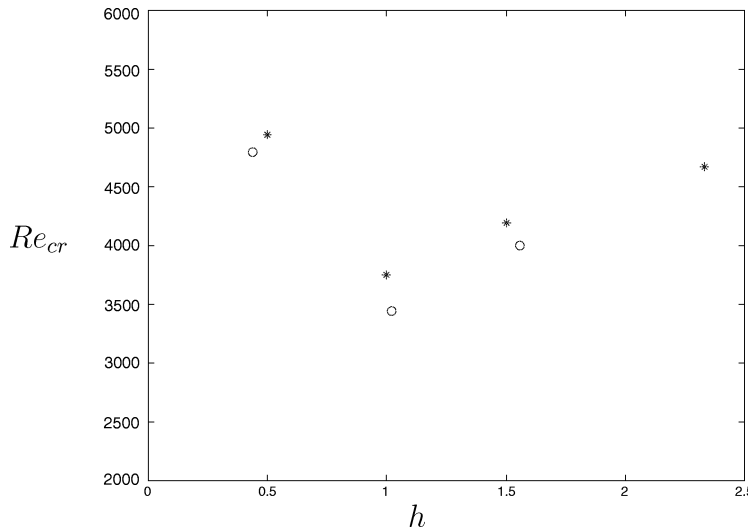

Figure 8. Critical Reynolds number versus aspect ratio. ∗: test cell I, $a = 0.16$, flat surface except the meniscus on the heater, o: test cell II, $a = 0.21$, flat surface.

might be due to increasing effects of buoyancy with increasing aspect ratio (as suggested by the criterion (14)), despite the fact that gravitational and thermocapillary forces act in the same direction, since the primary effect of buoyancy might be to establish a stable stratification in the interior, [36].

A combination of two effects is responsible for the lower critical numbers found with test cell II compared to cell I. First the heater radius in cell II is larger so that the heat flux to the fluid is greater and the appearance of the oscillation occurs at lower temperature. The larger delivery of heat to the fluid could also mean a larger influence of buoyancy. Secondly, the small meniscus on the heater present in cell I is known to stabilize the flow, as discussed above. Still the difference between the results obtained in the two cells is less than 8%.

The increase in critical Reynolds number for aspect ratios larger than unity is in disagreement with the results of Kamotani [14] where the critical difference of temperature decreases monotonically with aspect ratio. The significant differences between the two experiments are that the Prandtl number was 27 instead of 14, and that the heater radius was smaller in [14]. This could mean that buoyancy is less significant for higher aspect ratios in [14] than in our experiment, as discussed above.

4.3. Supercritical oscillations

Here we will describe the structure and features of supercritical oscillations, beyond the onset of oscillations described in the previous section. In order to characterize the oscillations, the amplitude, frequency and the phase of a temperature signal recorded close to the surface were studied. A typical signal for an oscillatory flow is shown in *figure 9*.

The amplitude of the temperature signal was obtained from a spectral analysis. Using FFT the power spectral density of the signal was computed, and from this the amplitude was obtained as twice the square root of the area of the peak corresponding to the fundamental frequency.

From the amplitudes A measured for increasing Reynolds numbers the critical Reynolds number for the onset of the instability can be assessed. The search for the onset of the oscillation was performed both by increasing the Reynolds number and decreasing it in order to check for any hysteresis. No hysteresis was detected indicating that the bifurcation was of supercritical type. According to the bifurcation analysis the

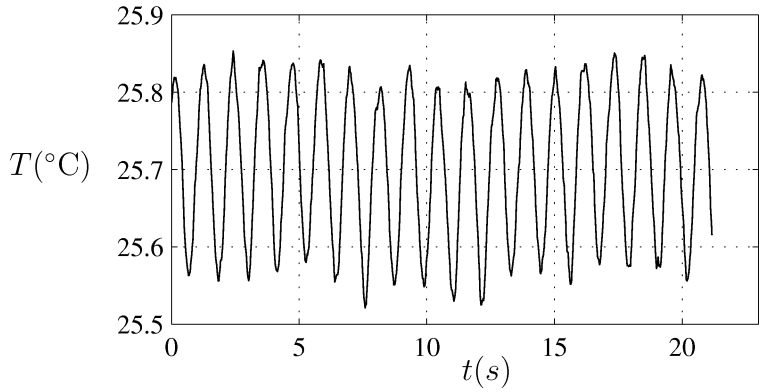

Figure 9. Surface temperature at $r = 0.56$, $\Delta T = 12.4°\mathrm{C}$.

amplitudes of the oscillations should grow proportionally to the square root of $(Re - Re_{cr})$ for a supercritical bifurcation. Hence

$$A = C\left(\frac{Re - Re_{cr}}{Re_{cr}}\right)^{1/2}. \tag{15}$$

The parameters C and Re_{cr} were computed by curve fitting using a Nelder–Mead type simplex search method.

Increasing the Reynolds number above the onset of oscillations involves a change of the features of the temperature oscillation. *Figure 10* shows the nondimensional amplitudes as a function of the parameter $\varepsilon = (Re - Re_{cr})/Re_{cr}$, which will be referred to in the following as the reduced Reynolds number. The top left insert in *figure 10* shows the simulated time signal for a slightly supercritical case, $\varepsilon = 0.04$, which is seen to have a sinusoidal shape, as expected this close to criticality. The signal in the middle insert, $\varepsilon = 0.3$, is slightly deformed by the overtones which start to appear. Finally the top right signal for a well overcritical case ($\varepsilon = 0.6$) shows a visible first harmonic. Both experiments and simulations show an increase of the amplitude, along a $1/2$ slope, in agreement with bifurcation theory. For $\varepsilon > 0.4$ in the simulation the amplitude shows a smaller increase with *Re*, i.e. a saturation. The discrepancy observed between the experiment and the simulation concerning the level of amplitude is due to a sligthly different position for the measurement. The temperature sensing part of the cold-wire was actually located just below the free surface whereas the temperature in the simulation is obtained at the surface.

As a detailed comparison between simulation and experiment, we determined the critical Reynolds number from simulations and experiment for a particular set of parameters. Using the method described above the experimental critical Reynolds number was found to be equal to 3150 for $Pr = 14$, $h = 1$, $a = 0.21$, and a flat surface without meniscus on the heater. The temperature was measured at the nondimensional radius $r = 0.56$. The conditions in the simulation were similar, except for the radial position where the temperature was recorded, which was at $r = 0.6$ instead of 0.56. The values found in experiments and in simulations are summarized in *table III*, and show a satisfactory agreement between experimental and numerical critical Reynolds numbers as well as frequencies at onset. In conclusion, the good agreement found between the critical numbers for oscillation shows that the mathematical model without surface deformation and without heat losses is accurate, and that the experimental parameters are well calibrated.

When the Reynolds number is increased further above the critical Reynolds number the nonlinear behaviour of the oscillation increases significantly. The nonlinear self-interaction of the dominant mode generates harmonics. In *figure 11* a comparison between experiment and simulation is reported for a supercritical case with $\varepsilon = 0.6$. In the upper panels the nondimensional temperatures are compared. One can notice that the

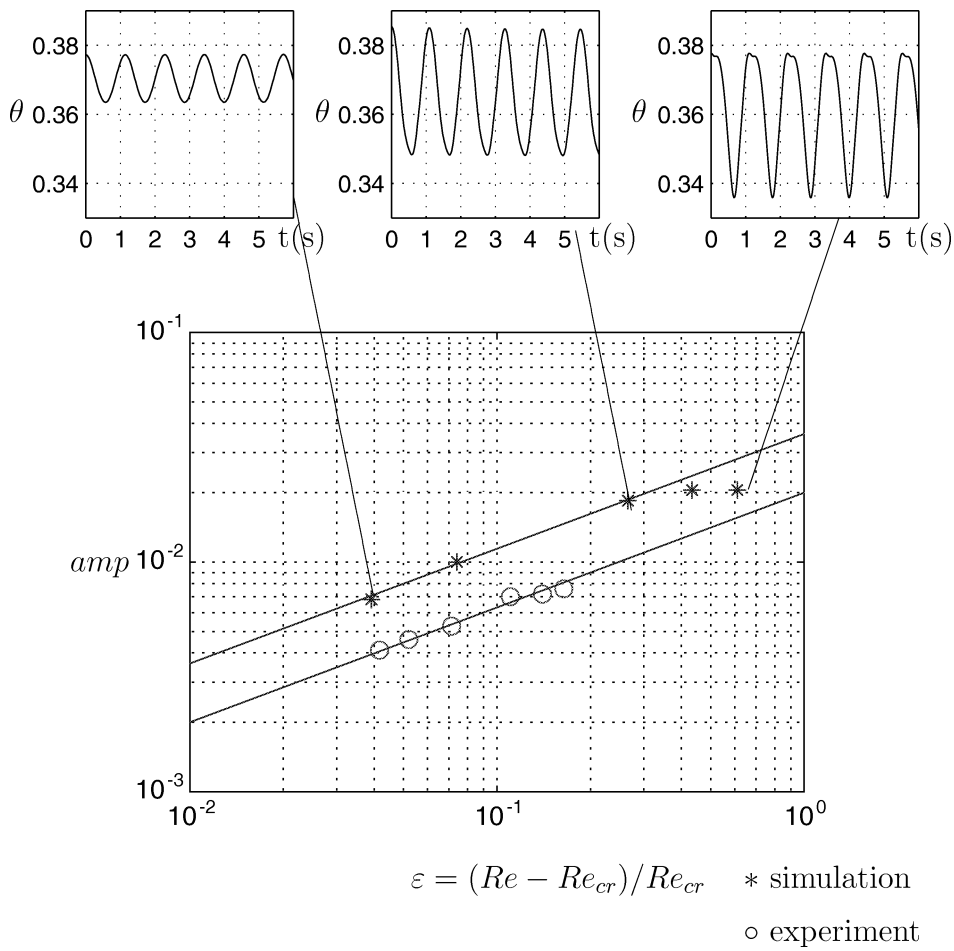

Figure 10. Non-dimensional amplitude of temperature oscillations (θ) versus the reduced Reynolds number (ε).

Table III. Characteristics of the instability for experiment and simulation with $h = 1$, $a = 0.21$.

Case	Re_{cr}	ΔT_{cr}	f (Hz)	Azimuthal wavenumber
Experiment	3150 ± 50	11.4 ± 0.2	0.91 ± 0.05	3
Simulation	2900	10.4	0.88 ± 0.05	3

signals agree well in amplitude but are slightly shifted. This difference in the mean temperature is likely to be due to a slightly different axial location for the measurement.

When performing a Fourier analysis (*figure 11* lower panels) the fundamental frequency for the experiment is found equal to 0.91 whereas the simulation gives a value of 0.904.

The higher harmonics are more visible in the signal from the simulation than from the measurements. This is related to the phase between the fundamental frequency and the first harmonic and the strength of the first harmonic. In the experimental case the phase is equal to -0.11 radian indicating that the fundamental and the first harmonic are in phase. On the other hand the simulations exhibit a phase of 2.575 radian. Moreover the amplitude of the first harmonic is twice as large in the simulation as in the experiment. In general the phase of a signal is known to vary strongly in regions subjected to a large gradient in the mean value. In the present

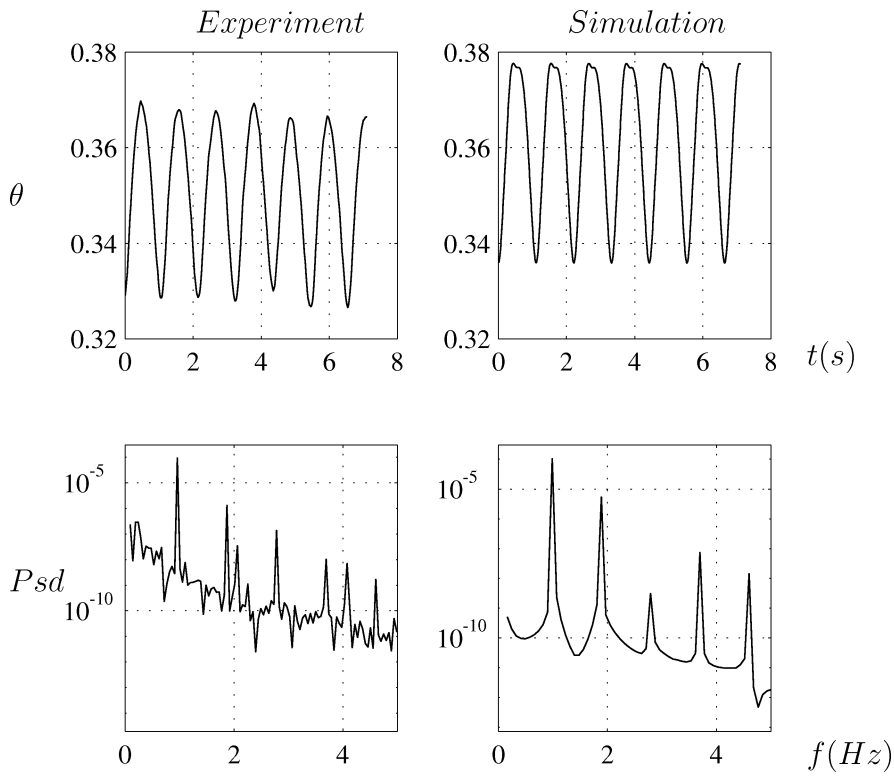

Figure 11. Upper panels show temperature signals at a point on the free surface for simulation and experiment, respectively. The lower panels show the power spectral density of the signals in the upper panels. The aspect ratio $h = 1$, the heater radius is $a = 0.21$. $\varepsilon = 0.61$ and the temperature was recorded at $r = 0.49$.

case the temperature varies strongly vertically in the boundary layer below the free surface. The discrepancies found are hence likely to be due to different vertical locations for the two signals.

4.4. Azimuthal wavenumbers

In order to characterize the spatial structure of the oscillatory state, the azimuthal wavenumber, and whether it is a standing or travelling wave in the azimuthal direction have to be assessed. It has been found experimentally and numerically in other configurations by several authors (Preisser et al., [9], Wanschura et al., [13], Levenstam and Amberg, [12], Velten et al., [10]), that the selection of azimuthal wavenumber depends strongly on the aspect ratio. In the geometry studied here, we have also found that the heater radius is important in determining the azimuthal wavenumber.

We have made simulations and experiments for different heater radii and different values of the parameter ε. *Figures 12* and *13* show flow visualization sequences of Mode 2 and Mode 3 respectively as visualized from above. In *figure 12* the heater aspect ratio is $a = 0.16$ whereas in *figure 13* it is $a = 0.21$. The centre part in the photographs has been covered by the grey area to facilitate the observation. The microscope is focused below the surface and the fluid is seeded with particles in order to visualize the flow field. The bright ring around the heater is reflected by particles which are oriented in the flow. The three photographs in each figure were taken in sequence clearly showing that the wave is travelling in both cases, anticlockwise in *figure 12* and clockwise in *figure 13*.

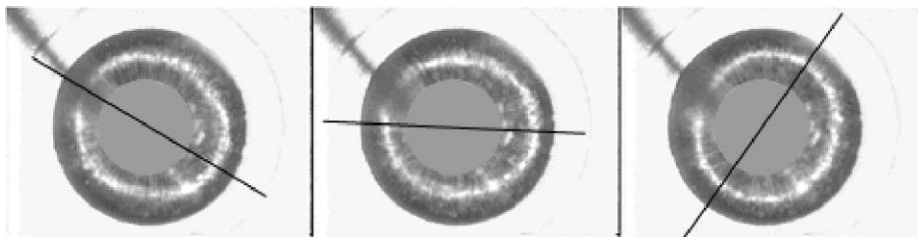

Figure 12. Mode 2, test cell I, $h = 1$, $a = 0.16$, $\varepsilon = 0.57$.

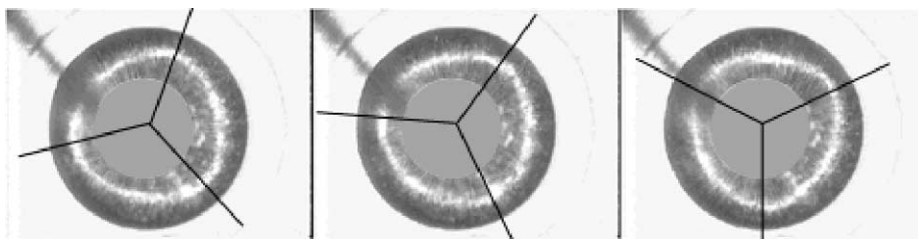

Figure 13. Mode 3, test cell I, $h = 1$, $a = 0.21$, $\varepsilon = 0.60$.

Figure 14 shows a sequence of simulated isotherms on the free surface for a case with a thin heater, $a = 0.08$. The motion can clearly be identified as a travelling wave with azimuthal wave number 2. The isotherms around the heater have been stretched out into ellipses which rotate around the heater. Hence the temperature disturbance field presents two warm regions and two cold ones in the azimuthal direction. This temperature field interacts with the flow field since forces are created towards the cold regions.

Figures 15 and *16* show similar sequences of the simulated surface isotherms, but for a thicker heater, $a = 0.21$. Both show an oscillatory mode with three temperature maxima in the azimuthal direction. Apparently, the increased value of a has caused the wavenumber 3 mode to become critical before wavenumber 2, and this dominates also in *figure 16*, significantly above critical conditions. The sequence in *figure 16* shows a distinct travelling wave, moving clockwise around the cell. The flow in *figure 15* which is closer to criticality, shows a pure standing wave, which is alternating periodically between two patterns separated by a 60° angle, passing through a perfectly axisymmetric flow.

We generally found standing waves for states close to criticality, and travelling waves for conditions that are sufficiently supercritical. This is a consistent with all of our observations. This is also in agreement with the numerical results of Savino and Monti [37], in a liquid bridge configuration. When performing these simulations great care has been taken to always allow a long simulation time so that the observed patterns are truly periodical and not slow transients. A simulation for a new parameter setting was started from the nearest available converged solution and was continued until the amplitude of the oscillations was unchanged over 10–20 periods. The case with $Re = 4650$ in *figure 16* was simulated up to a nondimensional time of 27900, corresponding to 54 s in dimensional time, or 0.43 in the very slow diffusive timescale R^2/α ($t = t^*U/R = t^*\alpha/R^2 \cdot RePr$, with definitions given above the nondimensional equations, equations (2) to (4)). The simulation times for the other cases are given in the captions to the figures.

The heater size was a sensitive parameter concerning the preferred mode. However, both mode 2 and 3 could occur for the same configuration of aspect ratio and heater ratio depending on other parameters like the surface shape, the disturbance of the free surface, etc. In some cases a mixed mode with both wave number 2 and 3 has

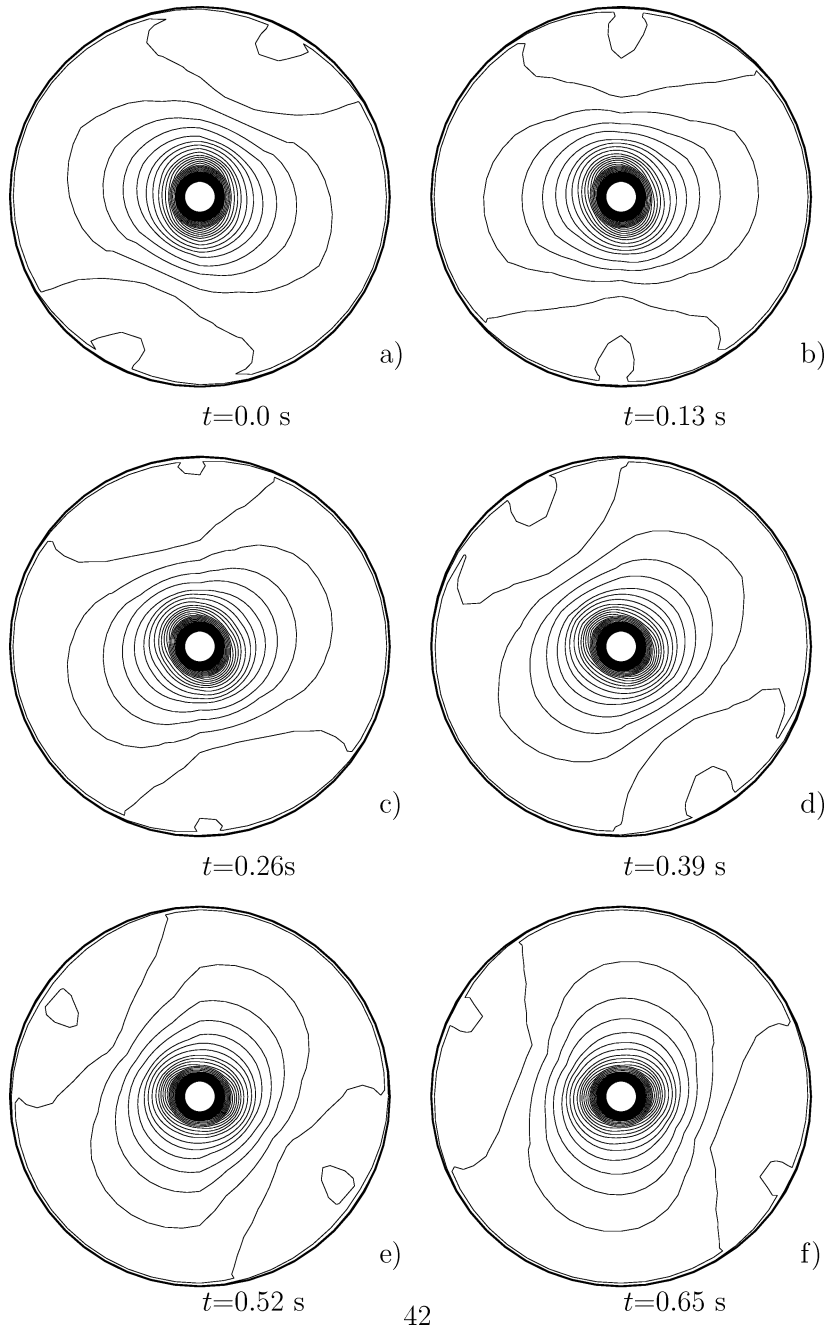

Figure 14. Surface isotherms from 0 to 1 for different times, $Re = 6922$, $Pr = 14$, $a = 0.08$, $\varepsilon = 0.62$. Total nondimensional simulation time was 16380.

been observed in both experiments and simulations. This state did indeed prevail over a long simulation time and did not seem to be a transient.

The aspect ratio h also influences the choice of the instability mode. The geometrically determining factor is the size of the core of the basic state vortex, relative to its circumference. By analogy to basic shear flows [13], or for small Prandtl numbers, to free vortex rings [12], the azimuthal wave number is seen to be approximately

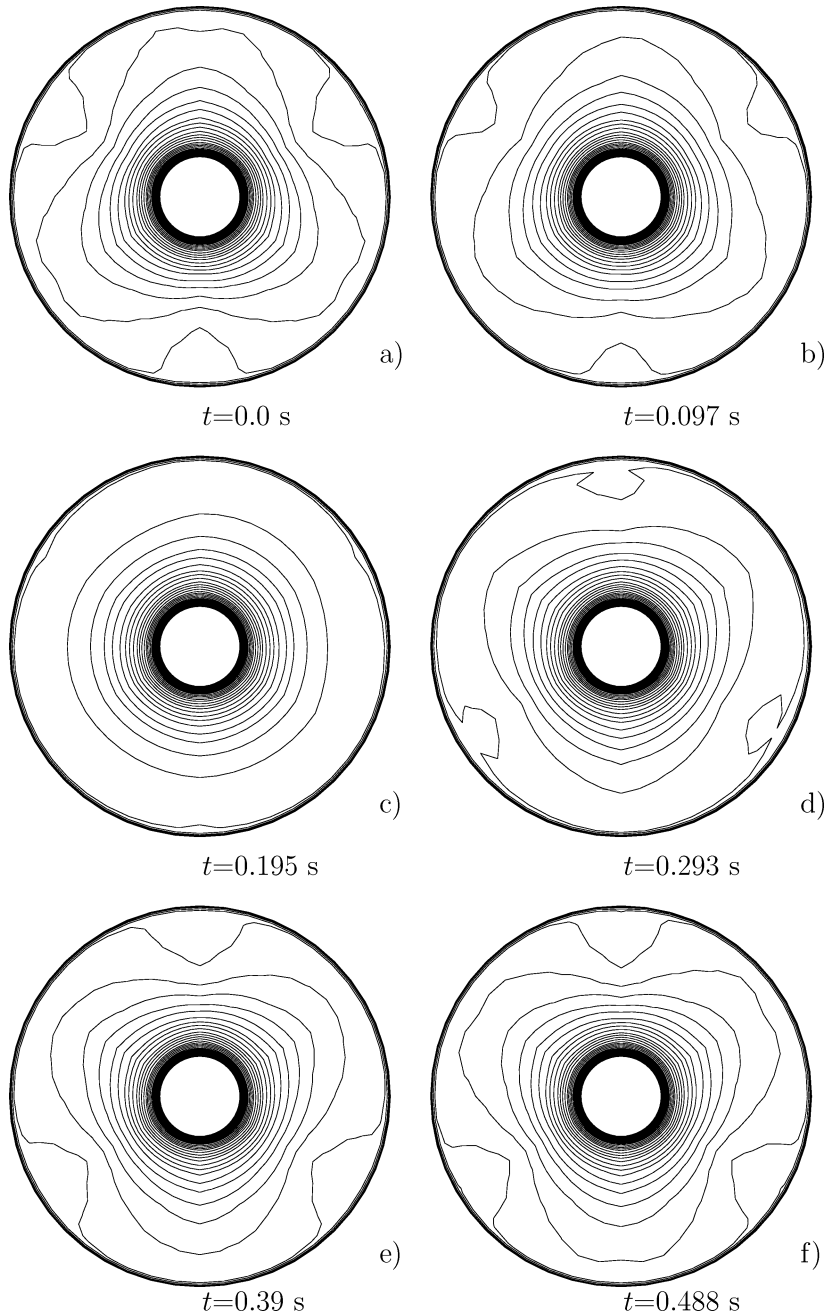

Figure 15. Surface isotherms from 0 to 1 for different times, $Re = 3650$, $Pr = 14$, $a = 0.21$, $\varepsilon = 0.26$. Total nondimensional simulation time was 9743.

equal to the number of vortex core radii that fit on an average vortex circumference. In half zones this mode selection is well known, [38,12,13], for both low and high Prandtl numbers. In this geometry however, there is an additional geometrical parameter, the influence of which can be understood in a similar way. A short cell (small h) with a thick heater (large a) would produce a basic flow with a relatively small vortex core compared to the vortex circumference and would thus promote higher azimuthal wave numbers whereas a long cell, or a

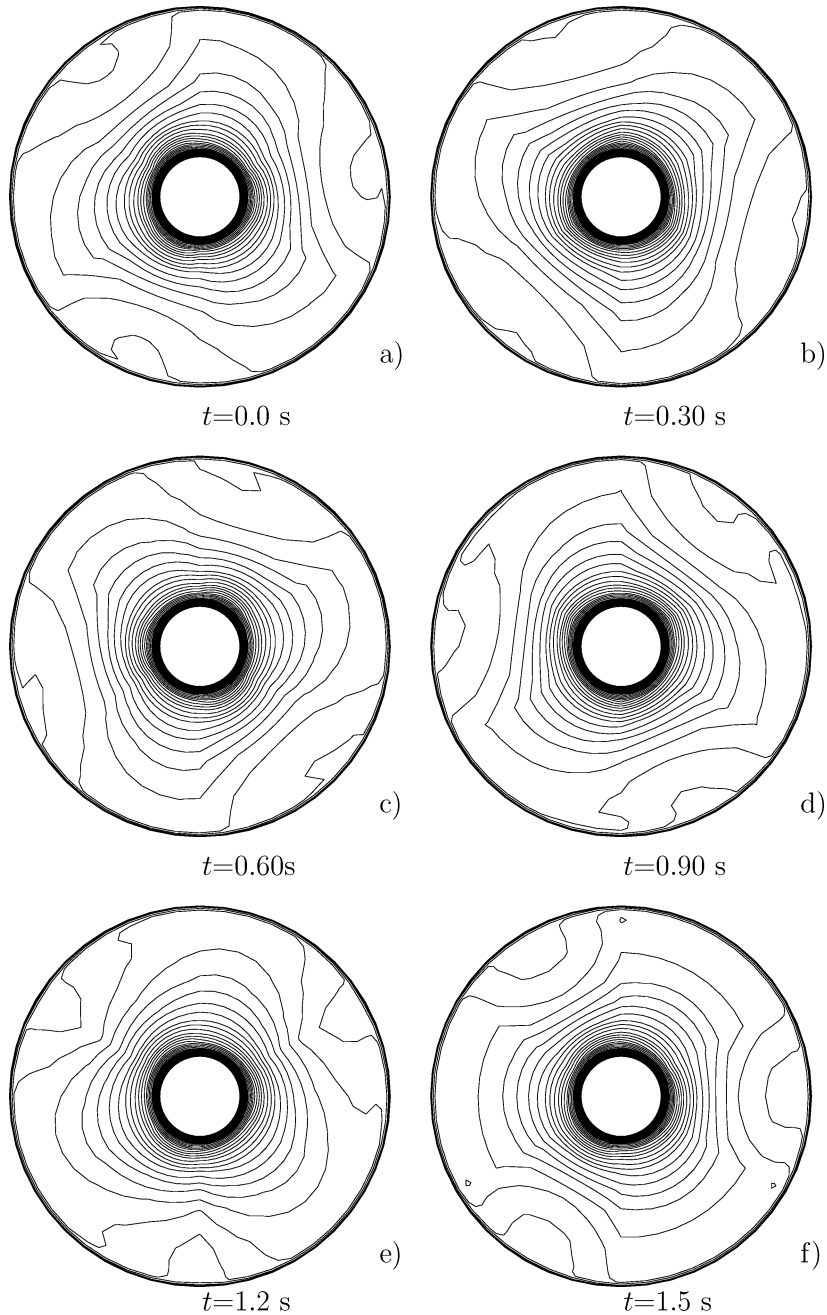

Figure 16. Surface isotherms from 0 to 1 for different times, $Re = 4650$, $Pr = 14$, $a = 0.21$, $\varepsilon = 0.61$. Total nondimensional simulation time was 27900.

thin heater gives preference to a lower mode. Note that Schwabe et al. [38] using very small h has identified a wavenumber as high as 13.

Kamotani and coworkers [14,21,22,18] have measured surface temperature distributions on the surface and have found generally very similar patterns as those shown in *figures 14* to *16*. Figure 15 in [18] shows a travelling wavenumber 2 mode and a standing wavenumber 3 mode, that look very similar to those shown here

in *figures 14* and *15*. For instance we note the tendency to form a cold patch near the outer rim that is visible in for instance *figure 15(d)*. They investigated the mode selection as a function of container size and temperature difference. In their experiment, with $a = 0.1$, the wavenumber was always 2 at onset, irrespective of container size. For the two larger size containers (2 and 3 cm diameters), the pattern was replaced by a wavenumber three mode in the nonlinear regime when $\Delta T/\Delta T_{cr} = 1 + \varepsilon$ was 1.4 and 1.5, respectively. Their experiments were made in microgravity so buoyancy was not responsible for the change of mode.

In our case the mode shape was clearly determined by the geometrical parameters, as discussed above. In view of our own results, a partial explanation for the mode change found in [18] could be that with $a = 0.1, h = 1$, the wavenumber 2 and 3 modes become critical almost simultaneously, with wavenumber 2 being only slightly less stable. Thus very small higher order effects may determine which is actually observed. The change from wavenumber 2 to 3 in the nonlinear range could be due to nonlinear changes of the mean flow that promote wavenumber 3 over 2. The dependence of mode shape on the container size could be due to any geometrical imperfection in one of the containers, or perhaps additional physical phenomena such as residual gravity or dynamic free surface deformations. Similarly, the selection of travelling or standing waves is due to nonlinear interactions between modes that can be very sensitive to higher order effects.

Our conclusion is thus that, since the details of the isotherms for instance in *figures 14* and *15* and those shown by Kamotani et al. in figure 15 of [18], are very similar, they are essentially the same instability and are due to the same mechanism. It is neither surprising nor contradictory however that, in a dynamically rich problem such as this, the selection of a particular mode may depend on higher order effects, such as residual gravity in space, or small buoyancy effects on earth, surface deformations, etc.

4.5. PIV measurements

So far we have mainly been investigating the thermal field in the oscillatory state. We now want to investigate the velocity field and try to relate it to the thermal field. With that motive in mind we performed PIV measurements of a vertical section of the cell II.

A well supercritical case was chosen, the Reynolds number is estimated to be equal to 6500. The corresponding reduced Reynolds number is $\varepsilon = 0.7$. A flat surface without meniscus on the heater was achieved. The aspect ratio is kept constant equal to 1 and $a = 0.21$. A sequence of velocity fields were captured with a time interval of 0.133 s (fastest recording time) and is shown in *figure 18*. The frames captured by the CCD camera were processed using an interrogation area of 64×64, corresponding to a physical size of $0.39 \times 0.39\ \mathrm{mm}^2$.

The postprocessing of the data showed that the seeding was not homogeneously distributed throughout the cell section. The particles tend to collect in the outer region of the vortex. A sedimentation effect is responsible for the inhomogeneous distribution. The particles employed have a rather large density ($2.8\ \mathrm{g/cm}^3$). Hence particles travelling in a region of low velocity tend to settle rapidly. This results in a lack of particles around the centre of the vortex, close to the outer wall and close to the bottom region and implies that these regions of the flow might give biased results. Moreover it is not expected to be possible to capture the flow near the free surface because of the large velocity gradients there, and shadowing by a rubber seal between the glass cylinder and the PVC top (see *figure 4*). Despite these sources of error, the measurements were able to capture the overall structure of the flow and to give quantitative velocity data in the outer region of the vortex.

The simulation used for comparison is a case with $Re = 4650$, which gives a corresponding $\varepsilon = 0.6$. The other parameters are the same as in the PIV-setup. The numerical velocity fields presented in *figure 17* were chosen so that they could be compared with the sequence of temperature fields of *figure 16*. The velocity fields are taken for an angle $\phi = 0$ (angle with the horizontal of the page).

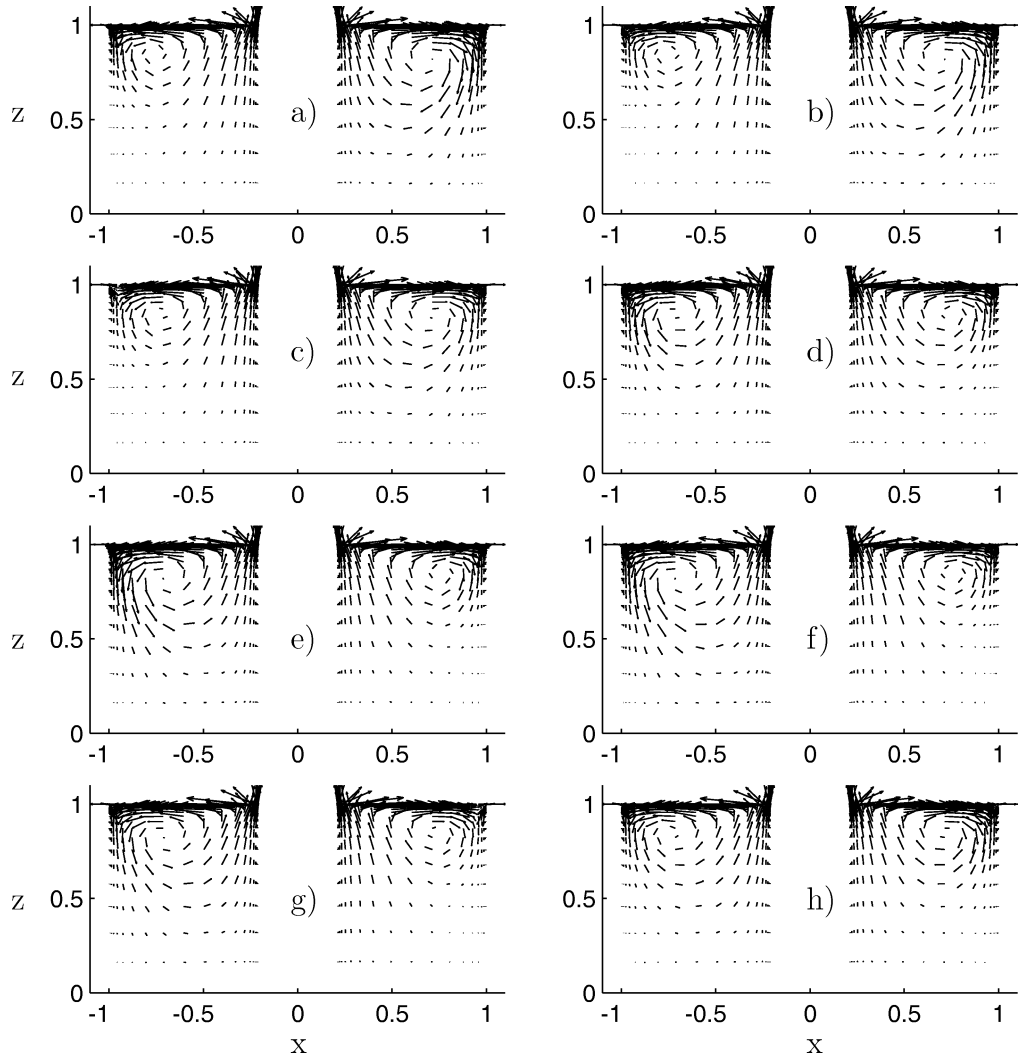

Figure 17. Simulations, $Re = 4650$, $h = 1$, $a = 0.21$. The azimuthal wavenumber of the instability is 3. The time interval between frames is 0.15 s. Each panel shows a cross section of the cell with height z versus horizontal coordinate $x = +- r$ (right side positive sign, left side negative). Panel (a) is for the same instant as the temperature field in *figure 16(b)*, panels (c), (e) and (g) correspond to *figures 16(c), 16(d)* and *16*, respectively.

The velocity sequences from PIV measurements (*figure 18*) and from simulations (*figure 17*) show a good agreement concerning the overall structure of the flow. The sequence shows a pulsation of the velocity field with acceleration and deceleration of the flow alternatively in both sides of the cell. The amplitude of the velocity oscillation is found smaller in the PIV-measurements than with numerical simulations.

The absolute velocity ($\sqrt{u^2 + w^2}$) at one point located in the backflow is presented for both PIV and numerical simulations in *figure 19*. Both signals exhibit an oscillation in time. The frequency of the oscillations are similar, whereas the amplitude does not agree well. Notice that the amplitude of the velocity oscillation depends strongly on the location. The amplitude of the velocity oscillation is large in the region close to the cold corner and in the region of descending flow. In contrast, the amplitude in the region close to the hot corner and the region close to the heater (where the flow moves upwards) is very small. The instability waves hence mainly disturb the outer region whereas the oscillation amplitude is quite small in the hot region.

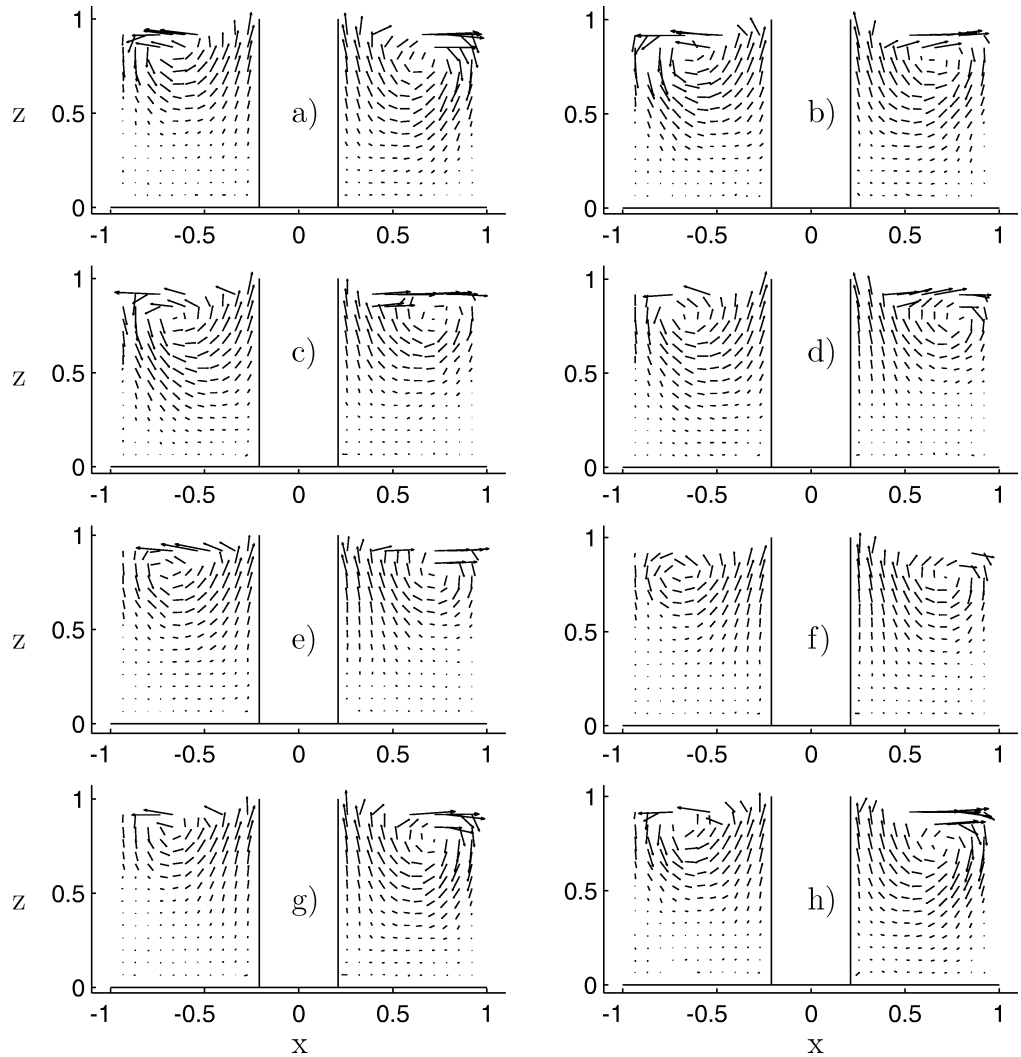

Figure 18. PIV, $Re = 6000$. Definitions of z and x as in *figure 17*. Time interval between fields: 0.133 s, $h = 1$, $a = 0.21$. The azimuthal wavenumber of the disturbance is 3.

5. Conclusions

Temperature and velocity measurements were performed, using a cold-wire technique and PIV measurements, respectively. Numerical simulations using an adiabatic flat free surface are shown to agree well with experiments. We could thus produce simulated flow and thermal fields, and corresponding experimental flow fields, using PIV. The existence of directly comparable simulations and experiments provides a detailed insight into the actual oscillatory motion, with the availablity of a simulation, and the integrity of an experiment. The instability is studied using both simulations and experiments in the nonlinear regime.

The agreement between the simulations and experiments, including the isotherm patterns in [18], that we have obtained shows that the physical effects that are modeled in the simulations are the ones responsible for the oscillatory flow. Thus we conclude that the oscillation mechanism only involves fluid inertia, thermocapillary forces and buoyancy. We have not found evidence that the deformation of the free surface plays a role in the

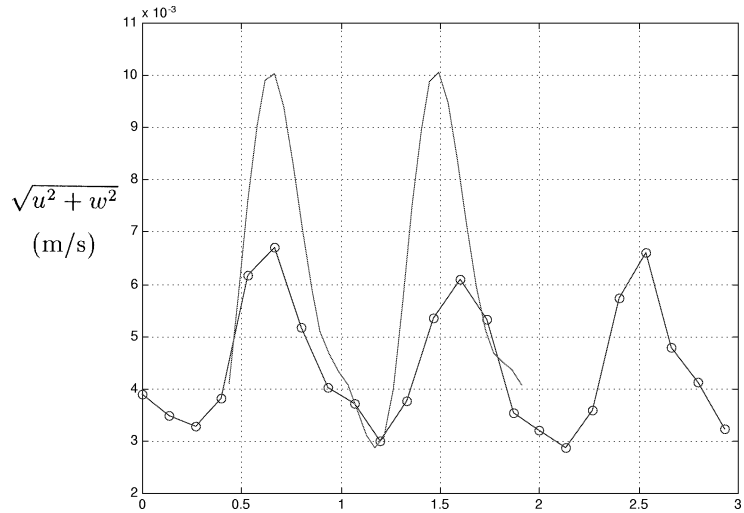

Figure 19. Velocity at one position of the backflow, simulation: solid line, $r = 0.807$, $z = 0.678$, PIV: ∘, $r = 0.816$, $z = 0.68$.

instbility mechanism. The static shape of the free surface is important, but only in establishing a different base state.

The preferred azimuthal wavenumber for the instability depends on the aspect ratio and on the size of the heater a and is expected to be approximately equal to the number of vortex core radii that fit on an average vortex circumference. A thin vortex ring (small h or large a) allows instabilities with relatively short wavelength whereas a thick ring (large h or thin heater, small a) gives preference to a lower mode with longer wavelength. This dependence on aspect ratio has been found previously for half zones, and the influence of the aspect ratio is here found to be analogous in the present geometry. It is also found here that the radius of the heater plays a similar role.

Finally the structure of the instability is analysed. An azimuthal thermal wave appears in the temperature field. There is a corresponding deformation of the basic toroidal vortex. Temperature and velocity fields are closely correlated.

The experimental procedures developed during the present work together with the accurate simulation tool are intended to be used to investigate methods to control the oscillations and even to suppress them.

Acknowledgements

This work was partially supported by the Swedish Research Council for Engineering Sciences (TFR). Our sincere thanks are also due to Marcus Gällstedt who built the test cells.

References

[1] Ostrach S., Low-gravity fluid flows, Annu. Rev. Fluid Mech. 14 (1982) 313–345.
[2] Schatz M.F., Neitzel G.P., Experiments on thermocapillary instabilities, Annu. Rev. Fluid Mech. 33 (2001) 93–127.
[3] Smith M.K., Davis S.H., Instabilities of dynamic thermocapillary liquid layers. Part 1. Convective instabilities, J. Fluid Mech. 132 (1983) 119–144.
[4] Smith M.K., Davis S.H., Instabilities of dynamic thermocapillary liquid layers. Part 2. Surface-wave instabilities, J. Fluid Mech. 132 (1983) 145–162.

[5] Xu J.-J., Davis S.H., Liquid bridges with thermocapillarity, Phys. Fluids 26 (1983) 2880–2886.
[6] Xu J.-J., Davis S.H., Convective thermocapillary instabilities in liquid bridges, Phys. Fluids 27 (1984) 1102–1107.
[7] Smith M., Instability mechanisms in dynamic thermocapillary liquid layers, Phys. Fluids 29 (1986) 3182–3186.
[8] Riley R.J., Neitzel G., Instability of thermocapillary-buoyancy convection in shallow layers. Part 1. Characterization of steady and oscillatory convection, J. Fluid Mech. 359 (1998) 143–164.
[9] Preisser F., Schwabe D., Scharmann A., Steady and oscillatory thermocapillary convection in liquid columns with free cylindrical surface, J. Fluid Mech. 126 (1983) 545–567.
[10] Velten R., Schwabe D., Scharmann A., The periodic instability of thermocapillary convection in cylindrical liquid bridges, Phys. Fluids 3 (1991) 267–279.
[11] Rupp R., Muller G., Neumann G., Three-dimensional time dependent modelling of the Marangoni convection in zone melting configurations for GaAs, J. Cryst. Growth 97 (1989) 34–41.
[12] Levenstam M., Amberg G., Hydrodynamical instabilities of thermocapillary flow in a half-zone, J. Fluid Mech. 297 (1995) 357–372.
[13] Wanschura M., Shevtsova V., Kuhlmann H., Rath H., Convective instability mechanisms in thermocapillary liquid bridges, Phys. Fluids 7 (1995) 912–925.
[14] Kamotani Y., Lee J., Ostrach S., An experimental study of oscillatory thermocapillary convection in cylindrical containers, Phys. Fluids A 4 (1992) 955–962.
[15] Kamotani Y., Chang A., Ostrach S., Effects of heating mode on steady axisymmetric thermocapillary flows in microgravity, in: Heat Transfer in Microgravity Systems, Trans. ASME, Vol. 290, 1994, pp. 53–59.
[16] Kamotani Y., Ostrach S., Pline A., A thermocapillary convection experiment in microgravity, J. Heat Trans-T ASME 117 (1995) 611–618.
[17] Kamotani Y., Ostrach S., Pline A., Analysis of velocity data taken in surface tension driven convection experiment in microgravity, Phys. Fluids A 6 (1994) 3601–3609.
[18] Kamotani Y., Ostrach S., Masud J., Microgravity experiments and analysis of oscillatory thermocapillary flows in cylindrical containers, J. Fluid Mech. 410 (2000) 211–233.
[19] Kamotani Y., Ostrach S., Pline A., Some temperature field results from the thermocapillary flow experiment aboard USML-2 spacelab, Adv. Space Res. 22 (1998) 1189–1195.
[20] Kamotani Y., Surface tension driven convection in microgravity, Adv. Astronaut. Sci. 96 (1997) 487–499.
[21] Kamotani Y., Masud J., Lee J.H., Pline A., Oscillatory convection due to combined buoyancy and thermocapillarity, AIAA-paper 95-0817, 1995.
[22] Kamotani Y., Masud J., Pline A., Oscillatory convection due to combined buoyancy and thermocapillarity, J. Thermophys. Heat Tr. 10 (1996) 102–108.
[23] Lin J., Kamotani Y., Ostrach S., An experimental study of free surface deformation in oscillatory thermocapillary flow, Acta Astronaut. 34 (1995) 525–536.
[24] Bäuerle L., Instability of thermocapillary convection in an open cylindrical container with heating at the center, M.Sc thesis, Dept. of Mechanics, KTH, 1994.
[25] Masud J., Kamotani Y., Ostrach S., Oscillatory thermocapillary flow in cylindrical columns of high Prandtl number fluids, J. Thermophys. Heat Tr. 11 (1997) 105–111.
[26] Neitzel G.P., Chang K.T., Jankowski D.F., Mittelmann H.D., Linear stability theory of thermocapillary convection in a model of the float-zone crystal growth process, Phys. Fluids 5 (1993) 108–114.
[27] Levenstam M., Amberg G., Winkler C., Instabilities of thermocapillary convection in a half-zone at intermediate Prandtl numbers, Phys. Fluids (2000) submitted.
[28] Levenstam M., Thermocapillary convection in floatzones, Technical Report TRITA MEK 1994:7, Department of Mechanics, KTH, 1994.
[29] Zebib A., Homsy G., Meiburg E., High Marangoni number convection in a square cavity, Phys. Fluids 28 (1985) 3467–3476.
[30] Shen Y., Neitzel G.P., Jankowski D.F., Mittelmann H.D., Energy stability of thermocapillary convection in a model of the float-zone crystal-growth process, J. Fluid Mech. 217 (1990) 639–660.
[31] Lavalley R., Experimental and numerical investigation of thermocapillary instabilities, Technical Report TRITA MEK 1997:20, Department of Mechanics, KTH, 1997.
[32] Johansson L.-L., The surface tension and its temperature dependence – an experimental technique, M.Sc Thesis TRITA MEK 1996:6, Dept. of Mechanics, KTH, 1996.
[33] Ostrach S., Motion induced by capillarity, in: Physicochemical Hydrodynamics (Advanced, London), Vol. 2, 1977, pp. 571–589.
[34] Kamotani Y., Platt J., Effect of free surface shape on combined thermocapillary and natural convection, J. Thermophys. Heat Tr. 6 (1992) 721–726.
[35] Sumner L.B.S., Neitzel G.P., Fontaine J.-P., Dell'Aversana P., Oscillatory thermocapiilary convection in liquid bridges with highly deformed free surfaces: Experiments and energy-stability analysis, Phys. Fluids A 13 (2001) 107–120.
[36] Carpenter B.M., Homsy G.M., Combined buoyant-thermocapillary flow in a cavity, J. Fluid Mech. 207 (1989) 121–132.
[37] Savino R., Monti R., Oscillatory Marangoni convection in cylindrical liquid bridges, Phys. Fluids 8 (1996) 2906–2922.
[38] Schwabe D., Möller U., Scheinder J., Scharmann A., The instability of shallow dynamic thermocapillary liquid layers, Phys. Fluids A 4 (1992) 2368–2381.